Monthly Notices
of the
ROYAL ASTRONOMICAL SOCIETY

MNRAS **475,** 2743–2753 (2018)
Advance Access publication 2017 December 8

doi:10.1093/mnras/stx3160

Mystery solved: discovery of extended radio emission in the merging galaxy cluster Abell 2146

J. Hlavacek-Larrondo,[1]★ M.-L. Gendron-Marsolais,[1] D. Fecteau-Beaucage,[1] R. J. van Weeren,[2] H. R. Russell,[3] A. Edge,[4] M. Olamaie,[5,6] C. Rumsey,[5] L. King,[7] A. C. Fabian,[3] B. McNamara,[8,9] M. Hogan,[8] M. Mezcua[1] and G. Taylor[10]

[1]*Département de Physique, Université de Montréal, Montréal, QC H3C 3J7, Canada*
[2]*Harvard-Smithsonian Center for Astrophysics, 60 Garden Street, Cambridge MA 02138, USA*
[3]*Institute of Astronomy, University of Cambridge, Madingley Road, Cambridge CB3 0HA, UK*
[4]*Centre for Extragalactic Astronomy, Department of Physics, Durham University, Durham DH1 3LE, UK*
[5]*Cavendish Laboratory, Battcock Centre for Experimental Astrophysics, JJ Thomson Avenue, Cambridge CB3 0HE, UK*
[6]*Imperial Centre for Inference and Cosmology(ICIC), Imperial College, Prince Consort Road, London SW7 2AZ, UK*
[7]*Department of Physics, University of Texas at Dallas, 800 West Campbell Road Richardson, TX 75080, USA*
[8]*Department of Physics and Astronomy, University of Waterloo, Waterloo, ON N2L 3G1, Canada*
[9]*Perimeter Institute for Theoretical Physics, Waterloo, ON N2L 2Y5, Canada*
[10]*Department of Physics and Astronomy, University of New Mexico, Albuquerque, NM 87131, USA*

Accepted 2017 November 1. Received 2017 October 23; in original form 2017 August 11

ABSTRACT

Abell 2146 ($z = 0.232$) is a massive galaxy cluster currently undergoing a spectacular merger in the plane of the sky with a bullet-like morphology. It was the first system in which both the bow and upstream shock fronts were detected at X-ray wavelengths (Mach ∼2), yet deep Giant MetreWave Telescope 325 MHz observations failed to detect extended radio emission associated with the cluster as is typically seen in such systems. We present new, multiconfiguration 1–2 GHz Karl G. Jansky Very Large Array (VLA) observations of Abell 2146 totalling 16 h of observations. These data reveal for the first time the presence of an extended (≈850 kpc), faint radio structure associated with Abell 2146. The structure appears to harbour multiple components, one associated with the upstream shock that we classify as a radio relic and one associated with the subcluster core that is consisted as being a radio halo bounded by the bow shock. The newly detected structures have some of the lowest radio powers detected thus far in any cluster ($P_{1.4\,\mathrm{GHz,\,halo}} = 2.4 \pm 0.2 \times 10^{23}$ W Hz^{-1} and $P_{1.4\,\mathrm{GHz,\,relic}} = 2.2 \pm 0.2 \times 10^{23}$ W Hz^{-1}). The flux measurement of the halo, as well as its morphology, also suggests that the halo was recently created (≈0.3 Gyr after core passage), consistent with the dynamical state of the cluster. These observations demonstrate the capacity of the upgraded VLA to detect extremely faint and extended radio structures. Based on these observations, we predict that many more radio relics and radio haloes in merging clusters should be detected by future radio facilities such as the Square Kilometre Array.

Key words: acceleration of particles – radiation mechanisms: non-thermal – shock waves – galaxies: clusters: individual: Abell 2146 – radio continuum general – X-rays: galaxies: clusters.

1 INTRODUCTION

Clusters of galaxies originate from the hierarchical mergers of subclusters and groups. As the structures collide, they can reach velocities of a few thousand km s^{-1} and kinetic energies in excess of 10^{64} erg. They are ideal laboratories for studying various physical processes, including key evidence of dark matter (Clowe, Gonzalez & Markevitch 2004; Markevitch et al. 2004; Bradač et al. 2006; Clowe et al. 2006) and non-thermal processes such as the generation of shocks and turbulence. However, in order to study these phenomena in detail, an inclination along the plane of the sky is needed, and having such a favourable angle is rare. Until recently, only a handful of such clusters were known,

★ E-mail: juliehl@astro.umontreal.ca

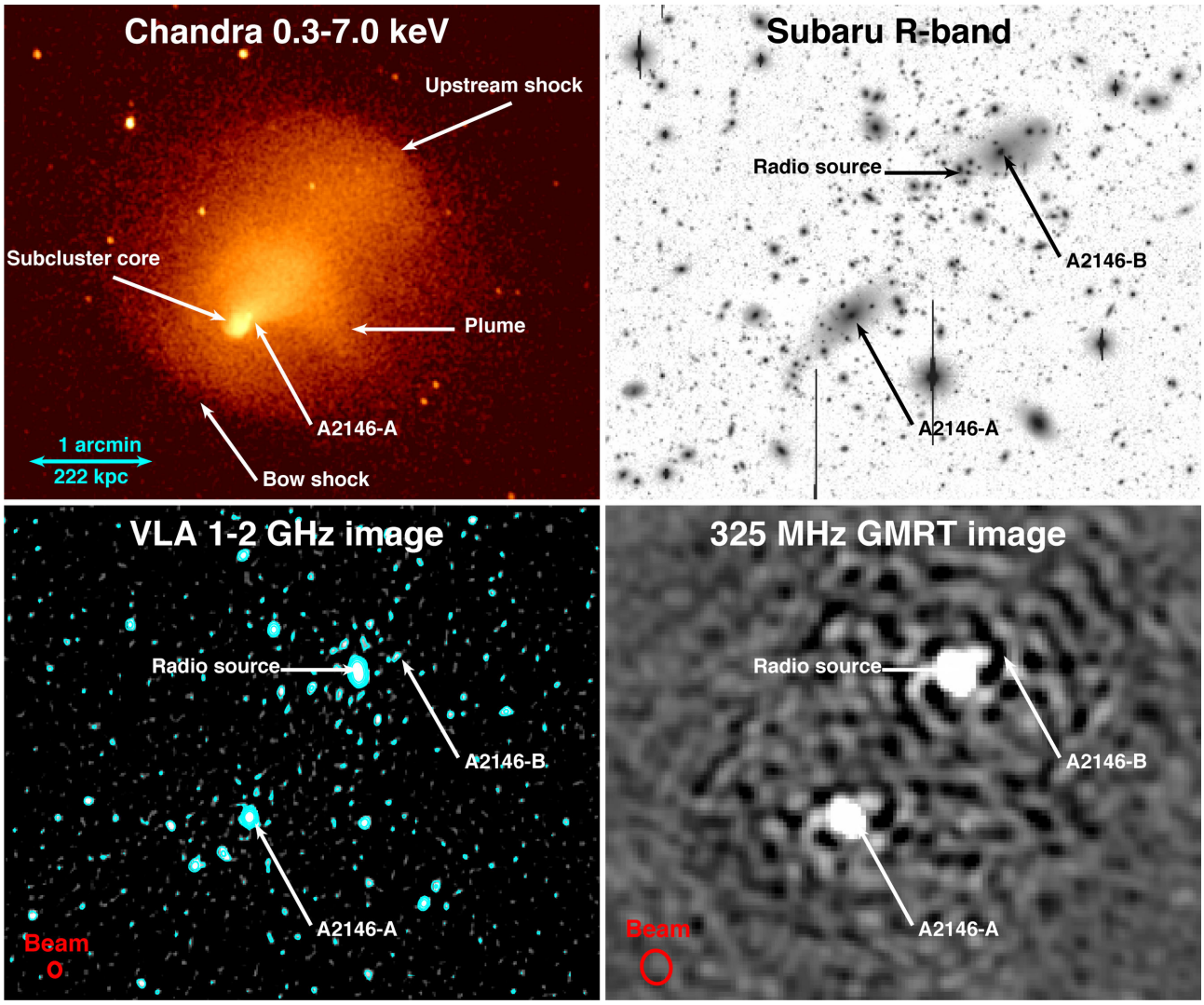

Figure 1. All images are on the same scale. Top left: *Chandra* image in the 0.3–7.0 keV band (418 ks) from Russell et al. (2012a), smoothed with a Gaussian function of 3 pixels. We highlight several features, including the two shock fronts and BCG A2146-A. Top right: Subaru Suprime-Cam image in *R* band from White et al. (2015). Bottom left: High-resolution 1–2 GHz VLA image, combining all data sets and configurations (see column 5 of Table 1 for details). The noise level in the vicinity of the cluster is $\sigma_{\rm rms} = 11$ μJy beam^{-1}, with a beam size of 3.9 arcsec × 3.2 arcsec. Contours levels are drawn at [1, 3, 9, 27, ...] × $3\sigma_{\rm rms}$ (8 levels in total). We highlight the location of the two BCGs (A2146-A and A2146-B), as well as the northern radio source that coincides with a member galaxy of the cluster. Bottom right: GMRT 325 MHz radio image from Russell et al. (2011). Note the remaining artefacts surrounding the A2146-A and the northern radio source. The beams for the radio images are shown in red in the lower left-hand corners.

including 1E 0657-55.8 (also known as the Bullet cluster; e.g. Markevitch et al. 2002), CIZA J2242.8+5301 (e.g. van Weeren et al. 2011), Abell 520 (e.g. Markevitch et al. 2005), and Abell 754 (e.g. Macario et al. 2011).

We have discovered another such cluster, Abell 2146 ($z = 0.232$, hereafter A2146; Russell et al. 2010, 2012b). It is undergoing a spectacular merger in the plane of the sky with a similar structure to the Bullet cluster. The *Chandra* image, shown here in the top left-hand panel of Fig. 1, reveals the remnants of a cool core (i.e. the bullet) being stripped of its gas and forming a tail of material leading back to a separate concentration of gas 400 kpc away. More importantly, the X-ray observations show that there are unambiguous density and temperature jumps associated with two X-ray shock fronts (Mach ∼2): one preceding the cool core (the bow shock) and another propagating outwards from the primary cluster (the upstream shock). Clear observations of shock fronts are extremely rare since they require the merger axis to be close to the plane of the sky so that projection effects do not smear out the surface brightness edges (see also Markevitch et al. 2002, 2005; Macario et al. 2011; Owers et al. 2011).

A2146 also hosts a brightest cluster galaxy (BCG; labelled A2146-A in Fig. 1) that is located 10 arcsec (≈40 kpc) behind the X-ray surface brightness peak, placing it behind the bow shock front. This is unexpected because cluster galaxies should be collisionless, as opposed to the hot intracluster gas that is slowed down by friction (e.g. Markevitch & Vikhlinin 2001). In a merger, the galaxies are therefore expected to precede the hot X-ray gas. This is not the case in A2146, and the location of the BCG1 is unlikely due

to projection effects since the observations of shock fronts require the merger axis to be close to the plane of the sky (see also White et al. 2015). Instead, Canning et al. (2012) and White et al. (2015) argue that it may be due to another galaxy perturbing the system, or that the merger is slightly off-axis.

Using 5.7 h of observations from the Giant MetreWave Telescope (GMRT) at 325 MHz, Russell et al. (2011) found no evidence of extended radio emission in A2146 down to an rms of 250 μJy beam^{-1}. The only two radio sources detected coincided with A2146-A and a second cluster galaxy to the north (labelled as *radiosource* in Fig. 1, see the bottom right-hand panel). Diffuse, cluster-wide radio emission is often seen in merging systems, classified as either radio haloes or radio relics depending on their morphology and polarization properties (see for a review Brunetti & Jones 2014). Radio relics are elongated, polarized structures that often trace shock fronts where particles are being re-accelerated (e.g. Ensslin et al. 1998). Radio haloes, on the other hand, are thought to originate naturally from shocks and turbulence generated during a merger. These amplify the magnetic fields and can re-accelerate existing populations of particles. This, in return, provides a source of non-thermal emission that can be seen at radio wavelengths (e.g. Brunetti et al. 2001; Petrosian 2001). Previous observations of cluster mergers have suggested a strong correlation between the radio power of haloes and the X-ray luminosity of the cluster, known as the L_X–P correlation (e.g. Liang et al. 2000; Cassano, Brunetti & Setti 2006). However, observations have shown that there is a bimodal population in this correlation. The cluster haloes with weaker radio power for a given X-ray luminosity are mostly thought to be the aged counterparts of those that follow the correlation (e.g. Donnert et al. 2013). The non-detection of a radio halo for A2146 by Russell et al. (2011) might therefore indicate that this cluster fits well into this aged population. However, this is inconsistent with the X-ray observations, since the estimated age from the shock fronts puts the cluster at an evolutionary stage of 0.2–0.3 Gyr after core passage (see Russell et al. 2010, 2012b; White et al. 2015), similar to the Bullet cluster, yet the Bullet cluster clearly sits along the correlation.

Radio haloes can also be produced by inelastic hadronic collisions between cosmic ray protons and thermal protons (see e.g. Dennison 1980). In this scenario, the radio luminosities of radio haloes should be around 10 times less than expected from re-acceleration models, providing a possible explanation for the weaker radio power sources in the L_X–P correlation (see also Brown et al. 2011). These models also predict that magnetic fields should be different in clusters with or without haloes and that radio halo hosting clusters should be gamma-ray luminous (e.g. Jeltema & Profumo 2011). Both of these predictions have not been observed (e.g. Bonafede et al. 2011; Ackermann et al. 2014).

Prior to A2146, all merging clusters of galaxies with X-ray-detected shock fronts had large diffuse radio emission associated with them. The non-detection in A2146 was therefore puzzling and deeper radio observations were needed to confirm the lack of extended radio emission. In this paper, we present new, multiconfiguration Karl G. Jansky Very Large Array (VLA) observations of A2146 at 1–2 GHz. In Section 2, we describe the observations, and then we present our main result in Section 3, the detection of extended radio emission in A2146. In Section 4, we discuss the implications of these results. Finally, in Section 5 we state our conclusions. Throughout this paper, we adopt $H_0 = 70\,\mathrm{km\,s^{-1}\ Mpc^{-1}}$ with $\Omega_m = 0.3$, $\Omega_\Lambda = 0.7$, resulting in a scaling of 3.698 kpc per arcsec at the redshift of the cluster ($z = 0.232$). All errors are 1σ unless otherwise noted.

2 OBSERVATIONS AND DATA REDUCTION

2.1 VLA observations

Four observations of A2146 were carried out in *L*-band on the VLA between 2012 March 16 and 2013 January 27 (P.I. Hlavacek-Larrondo). Two of these were in C-array, one in B-array, and one in D-array. The *L* band covers a frequency range from 1.0 to 2.0 GHz, with two 512 MHz IF pairs, each comprising 8 subbands of 64 MHz. We used the default integration time for the *L* band (3 s for B-array and 5 s for C-array and D-array). The data were recorded in 16 spectral windows, each subdivided into 64 channels. Full stokes correlations were recorded for a total acquisition time of 16 h. Details of each data set can be found in Table 1.

Data reduction was achieved using CASA (v.4.6.0), following the procedure described in the *L*-band tutorial found online on the NRAO website.[1] Briefly, malfunctioning antennas as well as radio frequency interference (RFI) were flagged based on the observation logs and visual inspection of the data sets. The data were then Hanning smoothed. After a first bandpass correction, automated flagging routines (TFCrop, RFlag) were applied. The data were calibrated using the normal calibration tasks (SETJY, delay and bandpass calibrations, gain calibration and flux scaling the gain solutions). The calibrations were then applied and the corrected data were splitted. For all observations, 3C286 was used as the primary calibrator, while J1634+6245 was used as a phase calibrator.

For each data set, three rounds of phase-only self-calibration were performed in order to improve calibration accuracy. Due to the high number of radio point sources, the software PYBDSM (v.1.8.6; Mohan & Rafferty 2015) was used in order to create island-type masks, which were inspected and included in the CLEAN process. For each of the imaging rounds during the self-calibration, we used Briggs et al. (1996) weighting, multifrequency synthesis (MS-MFS) with NTERMS = 2 (Rau & Cornwell 2011), and 480 W-projection planes (Cornwell, Golap & Bhatnagar 2005). We also used the ROBUST factor set to −0.5 for these images. The resulting properties, for each configuration, are shown in Table 1. Note that the noise level (rms) shown for all data sets represents the rms located near the cluster. When considering a region located far from the cluster, the rms was typically a factor of 2 smaller and reached the thermal noise level. We also note that the largest angular scales detectable are ≈8 arcmin for B-array, ≈70 arcmin for C-array, and ≈70 arcmin for D-array.

The final step consisted in merging the data sets together, and producing a final combined (B-array, C-array, D-array) image of the cluster. First, we combined the two measurement sets in C-array to produce a final image in that configuration. Here, the corrected column of each self-calibrated measurement set was split and then merged by running a CLEAN process. We then applied a long 10 min phase-only calibration and finally produced a combined image with CLEAN. The extra calibration step allowed us to correct for misalignments between the data sets. A similar procedure was then applied to data sets from all three configurations (B-array, C-array, and D-array), and a final, high-resolution image was produced (shown in the lower left-hand panel of Fig. 1). When producing this final image, we maximize the resolution (oversampling the beam by a factor of at least 3) and use BRIGGS weighting, MS-MFS with NTERMS = 2, 480 W-projection planes and a ROBUST factor of −0.5. The resulting rms near the cluster of this combined image is 11 μJy beam^{-1}, but

[1] https://casaguides.nrao.edu/index.php/Karl_G._Jansky_VLA_ Tutorials

Table 1. Radio observations of the merging galaxy cluster A2146.

	VLA B-array	VLA C-array	VLA D-array	Combined VLA	GMRT
Observing dates	2012 June 9	2012 March 16 2012 April 22	2013 January 27	...	2010 August 22
On source time	2.4 h	7.4 h	1.3 h	11.1 h	5.7 h
Correlations	Full stokes	Full stokes	Full stokes	Full stokes	RR and LL
Frequency	1–2 GHz	1–2 GHz	1–2 GHz	1–2 GHz	309 – 357 MHz
Beam size	3.7 arcsec × 2.9 arcsec	9.9 arcsec × 7.7 arcsec	47.1 arcsec × 30.0 arcsec	3.9 arcsec × 3.2 arcsec	9.3″ × 8.1″
Beam PA	−8.1deg	48.5 deg	28.0 deg	−3.7deg	10.7deg
rms	11 μJy beam^{-1}	11 μJy beam^{-1}	64 μJy beam^{-1}	11 μJy beam^{-1}	250 μJy beam^{-1}

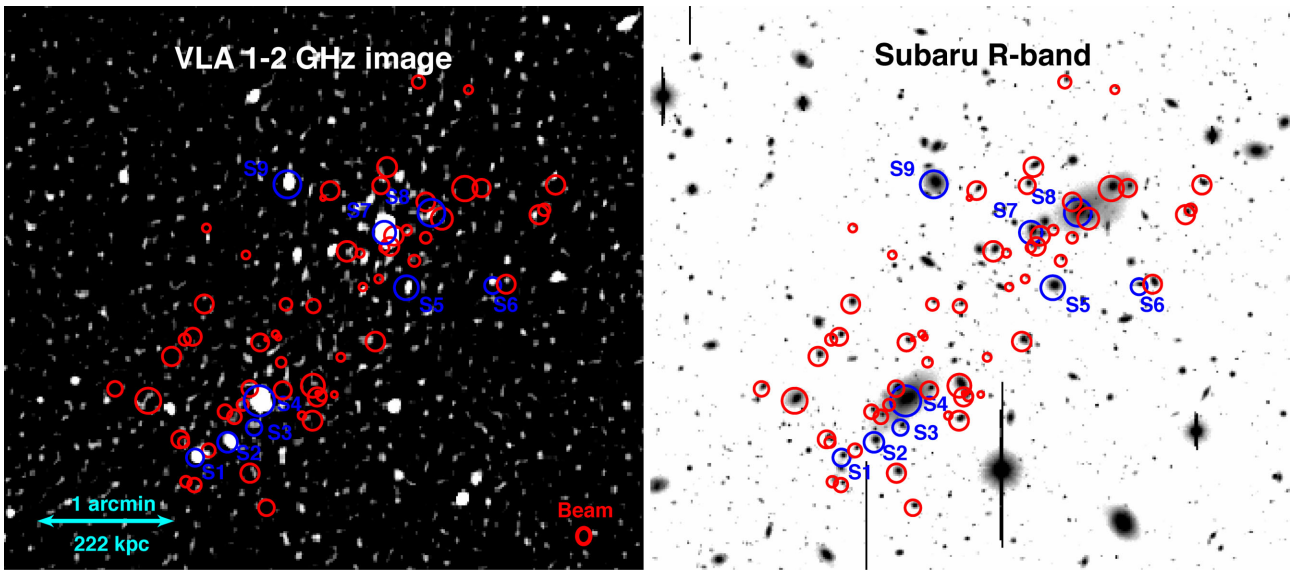

Figure 2. Left:High-resolution 1–2 GHz VLA image (same as in Fig. 1). In blue and red, we highlight the 68 spectroscopically confirmed cluster members found by White et al. (2015) and Coleman et al. (2017), The blue regions indicate those that coincide with a radio source detected above a $3\sigma_{\rm rms}$ level (labelled S1–S9 in the right-hand panel), where $\sigma_{\rm rms} = 11$ μJy beam^{-1}. Right: Subaru Suprime-Cam *R*-band image (same as in Fig. 1).

goes down to 5−6 μJy beam^{-1} when measured far from the source. Note that the final images were corrected for the primary beam.

2.2 GMRT observations

GMRT continuum observations were obtained at 325 MHz for A2146 on 2010 August 22 (5.7 h on source), and are presented in detail in Russell et al. (2011). These observations were taken with the software backend correlator with a total bandwidth of 32 MHz divided between 512 channels. The data were reduced using AIPS and the deepest image constructed gave an rms noise far from any sources of 92 μJy beam^{-1}, with beam size of 9.3arcsec × 8.1arcsec. However, the rms near the target goes up to 250 μJy beam^{-1} due to remaining artefacts in the image. The bottom right-hand panel of Fig. 1 shows the resulting image at 325 MHz. The observations are summarized in Table 1. Additional details regarding the data reduction can be found in Russell et al. (2011).

2.3 *Chandra* X-ray observations

Throughout this paper, we also make use of *Chandra* observations of A2146. The details of these observations can be found in Russell et al. (2012a). Briefly, A2146 was observed with the ACIS-I detector for a total of 377 ks (ObsIDs 10888, 12245, 13120, 12246, 13138, 12247, 13023, 13020, and 13021) and the ACIS-S detector for 39 ks (ObsID 10464). The data were processed, cleaned, and calibrated using CIAO (CIAOV4.3, CALDB 4.4.0), starting from the level 1 event file. Charge transfer inefficiency and time-dependent gain corrections were applied and flares were removed using the LC_CLEAN script. Data sets were reprojected to match the ObsID 12245 data set, combined and then exposure-corrected to produce the image shown in the top left-hand panel of Fig. 1. The net exposure time is 418 ks.

3 RESULTS

The bottom left-hand panel of Fig. 1 shows the deep 16 h 1–2 GHz VLA observations of A2146 at high resolution. This image was produced by oversampling the beam by a factor of at least 3. It was therefore designed to maximize the resolution and bring out point sources. This image reveals a multitude of radio point sources in the vicinity of the cluster. As in the GMRT 325 MHz image (the lower right-hand panel of Fig. 1), we detect both A2146-A and the northern bright source, but we also detect A2146-B at a faint $3\sigma_{\rm rms}$ level, where $\sigma_{\rm rms}$ is the local noise level. In addition, both A2146-A and the northern bright source appear to be extended compared to the beam size (shown in the bottom corner of the bottom left-hand panel of Fig. 1).

In Fig. 2, we show the same VLA image, along with the Subaru *R*-band image, but we highlight in red and blue the 68 spectroscopically confirmed cluster members found by White et al. (2015), as

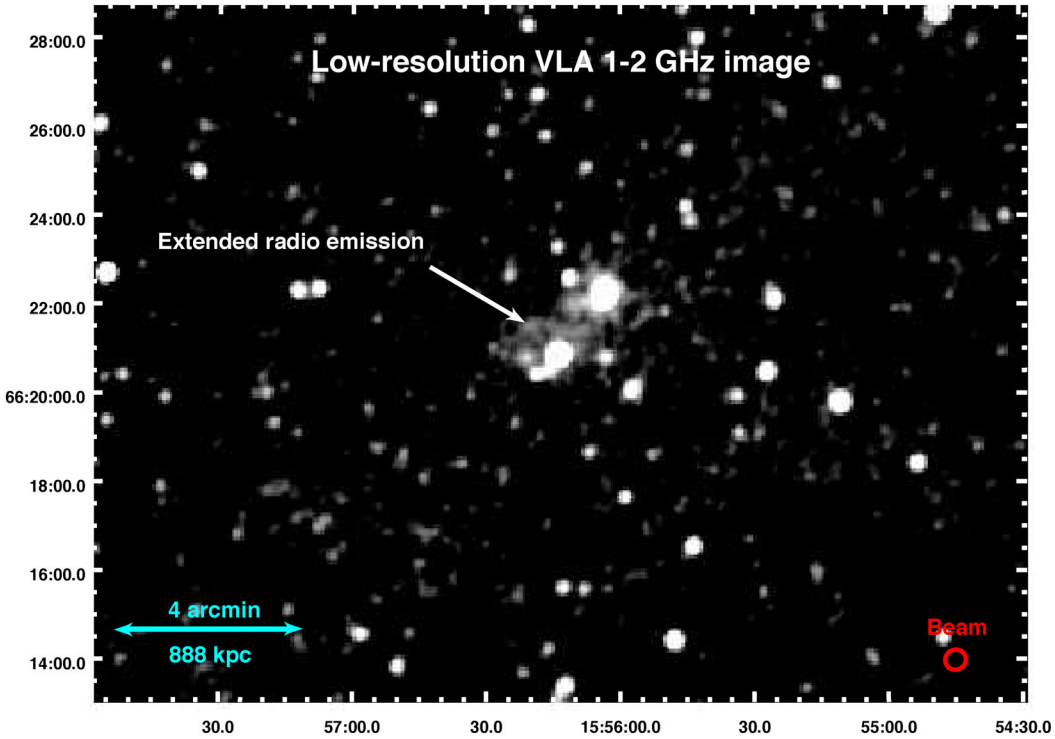

Figure 3. Large-scale low-resolution 1–2 GHz image obtained with the VLA observations, combining all data sets and revealing the presence of extended radio emission centred on A2146. The noise level is $\sigma_{\rm rms} = 12\,\mu$Jy beam^{-1}.

well as those from the strong lensing analysis by Coleman et al. (2017). We identify all cluster members that have a $3\sigma_{\rm rms}$ radio detection coincident with the galaxy centre. Nine of the 68 spectroscopically confirmed cluster members are detected at this level (shown with the blue regions), but we note that in addition to these nine sources, several other galaxies are detected at a $2\sigma_{\rm rms}$ level. In the discussion, we focus only on the $3\sigma_{\rm rms}$ detections.

When producing the VLA images shown in Figs 1 and 2, the parameters in the CLEAN task were chosen such that it would maximize the resolution. However, when imaged individually, both the VLA C-array and D-array data sets reveal the presence of radio emission that extend well beyond the beam in these images, indicating the presence of an additional faint and extended radio component associated with the cluster.

To demonstrate the existence of this radio component, in Fig. 3, we show the large-scale VLA image (B-array, C-array, and D-array), but at low resolution with a beam size of $14.1 \times 13.5\,{\rm arcsec}^2$ and position angle (PA) is of -27.5 deg. This image was created by applying an outertaper of 15arcsec, corresponding to a scale of 55 kpc, a ROBUST factor set to -0.25 and a cell size of 4arcsec. It highlights the presence of a faint radio structure that extends on the scale of the cluster, detected above a $3\sigma_{\rm rms}$ level where $\sigma_{\rm rms} \sim 12\,\mu$Jy beam^{-1}.

In Fig. 4, we show the same low-resolution VLA image, but zoomed-in on to the cluster on the scale of Fig. 2. We also show the projected temperature map from Russell et al. (2012b), created by extracting the temperature in binned regions reaching a signal-to-noise ratio of 32 ($\approx$1000 X-ray counts).

Finally, in Fig. 5, we show a point source subtracted VLA image. Here, we first create a point source only image by running a CLEAN task and applying a uvrange cut-off ($>1\,$kλ) while using a normal Briggs ROBUST factor set to 0. We then subtract this measurement set from the original data set using the task UVSUB. Finally, we image the point source subtracted data set while using a ROBUST factor set to 0, no inner uvrange cut-off and a uvtaper of 30arcsec. In all cases, clean boxes were used. This image reveals that the extended radio emission is actually composed of two components: a first extended component associated with the subcluster core and a second narrower component associated with the upstream shock. We also show the 0.3–7.0 keV unsharp-masked *Chandra* image, created by subtracting the X-ray images smoothed with a Gaussian σ of 5 and 20 arcsec, and then dividing the result by the sum of the two. This X-ray image shows nicely different features, in particular the two shock fronts as well as the plume to thesouth-west. It also shows that the diffuse radio structures are strongly bounded by the shock fronts. We discuss these features further in Section 4.

4 DISCUSSION

4.1 Compact radio sources

The original GMRT image at 325 MHz revealed the presence of two unresolved point sources: the BCG belonging to the subcluster core (A2146-A) and the northern bright radio source labelled as *radiosource* in Fig. 1. At 325 MHz, the first has an integrated flux of $S_{325\,\rm MHz} = 47 \pm 5$ mJy, while the latter has an integrated flux of $S_{325\,\rm MHz} = 93 \pm 9$ mJy (Russell et al. 2011).

The high-resolution 1–2 GHz image shown in Fig. 2 also reveals the presence of A2146-A ($S_{1-2\,\rm GHz} = 15.6 \pm 3.5$ mJy) and the northern bright radio source ($S_{1-2\,\rm GHz} = 36.6 \pm 4.0$ mJy), in agreement with the values reported by the 1.4 GHz NRAO VLA Sky Survey catalogue (NVSS; Condon et al. 1998). However, our new image shows that both of these sources are extended on scales of

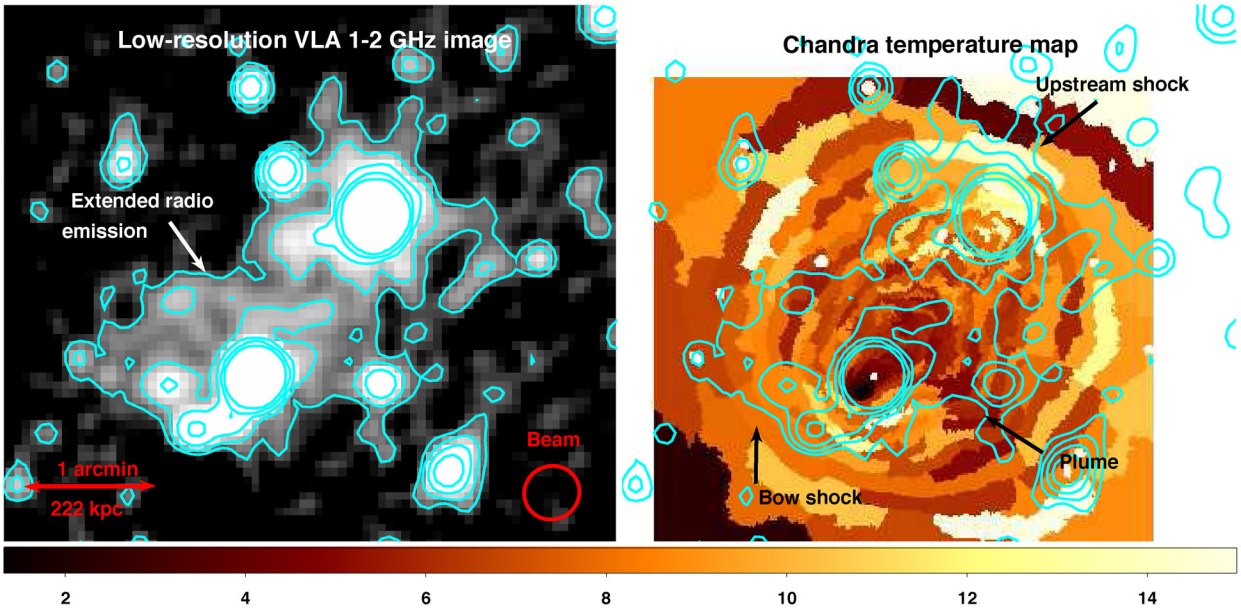

Figure 4. Left:Same low-resolution 1–2 GHz image as in Fig. 3, but zoomed-in on to the cluster on the same scale as Fig. 2. The five contours levels are drawn at [1, 2, 4, ...] × $3\sigma_{\rm rms}$, where $\sigma_{\rm rms} \sim 12$ μJy beam^{-1}. The beam size is 14.1 × 13.5 arcsec^2. Right: *Chandra* projected temperature map from Russell et al. (2012b). Same contours shown as in the left-hand panel. The colour bar reflects the temperature in keV units.

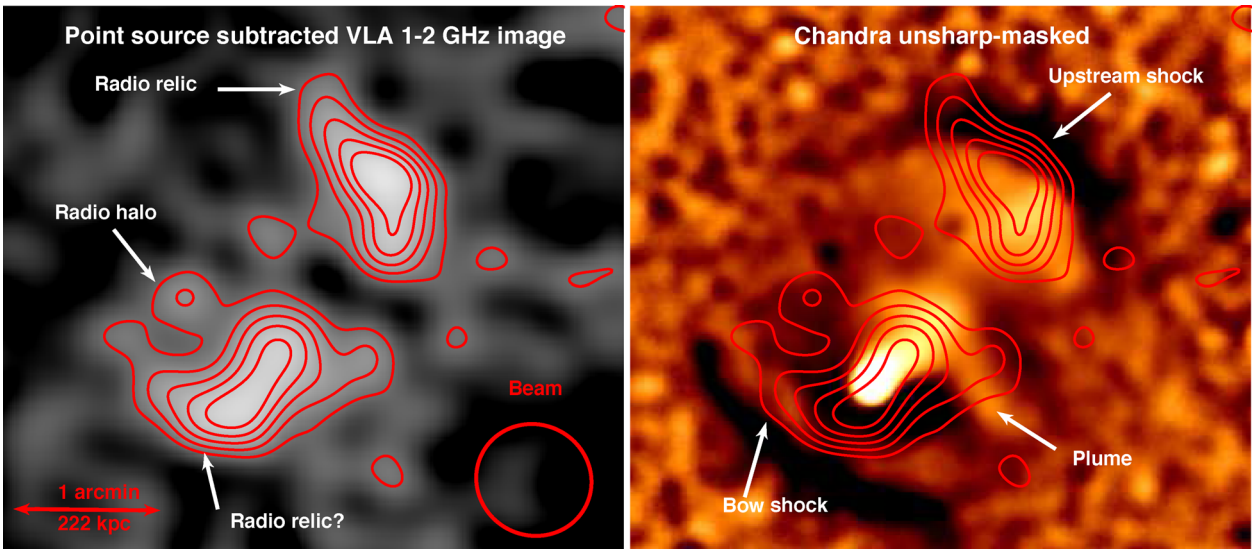

Figure 5. Left:Point source subtracted 1–2 GHz image on the same scale as Figs 2 and 4. The 6 contours levels are drawn at [3, 5, 7, ...] × $\sigma_{\rm rms}$, where $\sigma_{\rm rms} \sim 23$ μJy beam^{-1}. The beam size is 27.7 × 29.0 arcsec^2. Right: Unsharp-masked *Chandra* image in the 0.3–7.0 keV band.

37 kpc (10 arcsec; A2146-A) and 63 kpc (17 arcsec; northern radio source).

Both of these sources are not detected in the VLA Low Frequency Sky Survey (VLSS, rms ∼0.1 Jy beam^{-1}; Cohen et al. 2007). However, the reprocessed 150 MHz images obtained with the alternative TIFR GMRT Sky Survey (TGSS;[2] Intema et al. 2017) detects both A2146-A ($S_{150\,\rm MHz} = 29 \pm 8$ mJy) and the northern bright radio source ($S_{150\,\rm MHz} = 183 \pm 21$ mJy), although the first falls below the catalogue detection limit. Interestingly, the TGSS 150 MHz image also reveals that the northern radio source is extended and surrounded by faint 2σ radio emission. We include the values for the TGSS in Table 2. Finally, we include values at 5 GHz in Table 2 for A2146-A and the northern source, based on archival VLA observations (private communication, see also Hogan et al. 2015). We note that the 408 MHz images taken with the Westerbork Northern Sky Survey (WENSS; Haslam et al. 1982) detects the two radio sources but barely resolves them.

In Fig. 6, we show the spectral energy distribution of A2146-A (red points) and the northern bright source (blue points). The dashed lines show the expected flux density values for spectral indexes calculated between 325 MHz and 1.4 GHz for A2146-A ($\alpha = 0.7 \pm 0.2$) and between 150 and 325 MHz values for the northern source ($\alpha = 0.9 \pm 0.1$). This figure highlights two

[2] http://tgssadr.strw.leidenuniv.nl/doku.php

Table 2. Radio emission from A2146 cluster members. The type refers to compact (C) or extended (E). We also indicate in column 6 the flux density when detected at 325 MHz with the GMRT (Russell et al. 2011) and at 150 MHz with the TGSS.

Source	RA	Dec.	Type	$S_{1-2\,\mathrm{GHz}}$ (mJy)	Notes
S1	15:56:19.157	+66:20:25.860	C	0.26 ± 0.05	
S2	15:56:16.549	+66:20:33.260	C	0.18 ± 0.03	
S3	15:56:14.418	+66:20:40.350	C	0.05 ± 0.01	
S4 (A2146-A; BCG)	15:56:14.002	+66:20:53.220	E	15.6 ± 3.5	$S_{325\,\mathrm{MHz}} = 47 \pm 5$ mJy; $S_{150\,\mathrm{MHz}} = 29 \pm 8$ mJy; $S_{5\,\mathrm{GHz}} = 6.6 \pm 0.3$ mJy
S5	15:56:02.166	+66:21:47.770	C	0.08 ± 0.02	
S6	15:55:55.224	+66:21:48.819	C	0.06 ± 0.02	
S7 (northern source)	15:56:03.933	+66:22:14.410	E	36.6 ± 4.0	$S_{325\,\mathrm{MHz}} = 93 \pm 9$ mJy; $S_{150\,\mathrm{MHz}} = 183 \pm 21$ mJy; $S_{5\,\mathrm{GHz}} = 8.9 \pm 0.5$ mJy
S8 (A2146-B; BCG)	15:56:00.149	+66:22:23.940	C	0.08 ± 0.02	
S9	15:56:11.734	+66:22:37.690	C	0.6 ± 0.1	

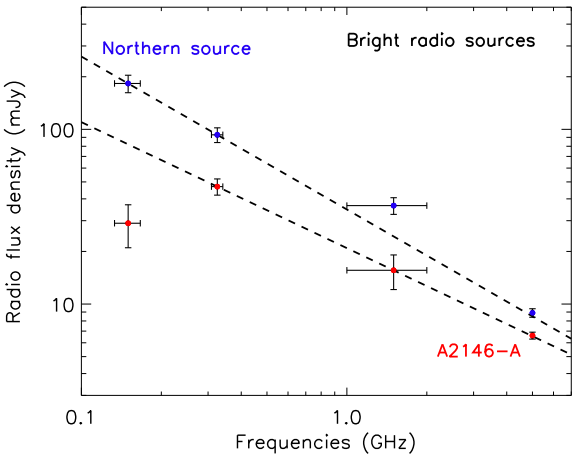

Figure 6. Left:Shown are the flux densities of the two bright radio sources in A2146: A2146-A (red points) and the northern bright source (blue points). The dashed lines highlight the expected fluxes when extrapolating from the measurements at 325 MHz and 1.4 GHz for A2146-A and from 150 and 325 MHz for the northern bright source.

important results: the spectrum of the northern source rolls over at high frequencies, indicative of synchrotron spectral ageing, and the spectrum of A2146-A turns over at ∼200–300 MHz. Such a turnover is characteristic of a Compton Steep Spectrum (CSS) source, which is usually associated with powerful compact radio sources in their early stages of formation. We note that O'Dea (1998) reported a correlation between frequency turnover and linear projected size for CSS and gigahertz peaked spectrum. For a turnover frequency of ∼200–300 MHz, the correlation predicts that A2146-A should extend no more than ≈30–40 kpc, which is just within the linear sizes we find for A2146-A.

The VLA image shown in Fig. 2 also reveals the presence of several other radio point sources not previously known. Nine of these radio sources coincide with known cluster members (labelled S1–S9 in Fig. 2), as identified by White et al. (2015) and Coleman et al. (2017). The radio fluxes of these galaxies are shown in Table 2. The only radio source that is also clearly detected at X-ray wavelengths is A2146-A (see Fig. 1).

A detailed analysis of the population of radio sources in A2146 will be conducted in a future paper (Hlavacek-Larrondo et al. in preparation). However, we note that A2146 appears to harbour an unusually large population of radio point sources (see King et al. in preparation), which may indicate that cluster mergers strongly affect their population of galaxies either through star formation or AGN emission that shines at radio wavelengths (e.g. Miller & Owen 2003; Poggianti et al. 2004).

4.2 Detection of extended radio emission

The original GMRT image at 325 MHz did not reveal the presence of a radio halo. This is not surprising considering that the GMRT is known to have problems in achieving high dynamic range images. Indeed, remaining artefacts in the form of ripples surrounding the two point sources could be seen in the original image (see the lower right-hand panel of Fig. 1), which increased the noise level to 250 μJy per beam in the inner regions. For a 1 Mpc source, Russell et al. (2011) found that the 3σ upper limit at 325 MHz for extended radio emission was 13 mJy determined as $3 \times \mathrm{rms} \times \sqrt{\mathrm{sourcearea/beam\,area}}$. Assuming a spectral index of $\alpha = 1$ defined such that $S_\nu \propto \nu^{-\alpha}$, Russell et al. (2011) further estimated that the 3σ upper limit was 3 mJy ($\sim 5.0 \times 10^{23}$ W Hz^{-1}) at 1.4 GHz.

Our new radio image reaches a noise level of ∼10 μJy beam^{-1}, which is an order of magnitude deeper than the GMRT image. This has allowed us to discover that A2146 hosts a large extended radio structure that may harbour multiple components, one associated with the subcluster core to the south-east and another associated with the upstream shock to the north-west. As shown in Figs 4 and 5, the radio emission is centrally located within the cluster and has a morphology that extends along the merger axis of the merger (north-west to south-east) with no clear association with individual galaxies. Considering both components, it has a largest linear size of ∼850 kpc and sharp edges that coincide with both the bow and upstream X-ray shock fronts. Such edges have also been observed in other merging clusters including the Bullet cluster (see Shimwell et al. 2014).

We note that the literature has reported the existence of several elongated, highly polarized arc-like radio structures known as radio relics (see for a review Brunetti & Jones 2014). These relics are thought to trace the outward going shock fronts produced by the cluster mergers (e.g. Ensslin et al. 1998, and references therein). One possible solution involves Diffusive Shock Acceleration (DSA) in which electrons from the thermal pool of particles go through several collisions across the shock fronts (e.g. Drury 1983). However, DSA is known to have several issues and van Weeren et al. (2017) recently argued that relics originate from the re-acceleration of fossil relativistic electrons from past active galactic nuclei outflows, based on the discovery of a direct connection between a radio relic and a radio galaxy in the merging galaxy cluster Abell 3411-3412. Several clusters with X-ray-detected shock fronts host such relics coincident with the shocks (e.g. Macario et al. 2011; Ogrean & Brüggen 2013).

In the case of A2146, the elongated morphology of the north-west radio component, as well as its strong association with the upstream shock as shown in Figs 4 and 5, leads us to surmise that this structure

is most likely a radio relic (Markevitch 2010; Macario et al. 2011; van Weeren et al. 2016). Based on our current understanding of radio relics from van Weeren et al. (2017), the fossil electrons from this relic may have originated from the bright northern radio source in A2146 (labelled as S7 in Fig. 2), but higher resolution images are needed to confirm this association.

The origin of the south-east radio component is however more uncertain. Figs 1 and 4 show that A2146 harbours a cool core that has survived the merger. This cool core also appears to coincide with the south-east radio component, implying that the radio emission seen to the south-east could originate from a classical mini-halo associated with the cool core. However, given the clear nature of the merger in A2146, the extended morphology of the south-east radio component (∼300 kpc) and the fact that many haloes (as opposed to mini-haloes) appear to align with their subcluster cores, we conclude that the south-east radio component is most likely not associated with a mini-halo. Instead, we argue that it is most likely associated with a radio halo either bounded by the bow shock (as often seen, e.g. Shimwell et al. 2014) or composed of a halo and a second relic that coincides with the bow shock (e.g. van Weeren et al. 2010). It could also consist of an unusual large box-like relic, such as the one seen in A2256 (Owen et al. 2014), but this would imply that the second relic extends significantly in the downstream region of the shock front given that A2146 is undergoing a merger in the plane of the sky. We therefore favour the interpretation in which the south-east radio structure is composed of a halo or a halo and relic. Since relics are known to be highly polarized compared to haloes, resolved polarization measurements could provide valuable information, but we note that the instrumental set-ups of the VLA observations were not designed to do these measurements. The resolution of the current VLA images are also not sufficient to determine if the radio structure seen to the south-east actually harbours multiple components. In summary, future observations will be required to determine the precise nature of the south-eastern component. For now, given its morphology and association with the subcluster core, we consider this structure to be a radio halo.

As shown in Fig. 5, the radio halo (south-eastern component) and relic (north-western component) are very faint and were only detectable through the very deep VLA images. To estimate the radio powers, we measure the total emission detected above $3\sigma_{\rm rms}$ in Fig. 5. We find that the halo has a flux density of $S_{1.4\,\rm GHz} = 1.5$ mJy, whereas the relic has a flux density of $S_{1.4\,\rm GHz} = 1.1$ mJy. We then compute the k-corrected radio power using $P_{1.4\,\rm GHz} = 4\pi S_{1.4\,\rm GHz} D_{\rm L}^2 (1+z)^{-(-\alpha+1)}$ (see van Weeren et al. 2014). For the halo, we use the derived spectral index of $\alpha \approx 1$ where $S \propto \nu^{-\alpha}$, see below, but stress that even if we used a value of $\alpha \approx 2$, the flux would only change at the 20 per cent level. For the relic, we use the derived spectral index of $\alpha \approx 2$. Following Cassano et al. (2013), we estimate the error on the flux density, and thus the radio power, as

$$\sigma_{\rm S_{Halo}} = \sqrt{(\sigma_{\rm cal} S_{\rm halo})^2 + ({\rm rms}\sqrt{\rm N_{beam}})^2 + \sigma_{\rm sub}^2}, \quad (1)$$

which considers the uncertainties on the flux density scale ($\sigma_{\rm cal}$), typically on the order of 5 per cent, and the noise level of the image (rms = 23μJy beam^{-1}) weighed by the number of beams within the structures. We do not consider $\sigma_{\rm sub}$, the uncertainty when removing the point sources, since the point sources have already been removed in Fig. 5. Overall, we find that the point-source subtracted k-corrected radio power of the halo (south-eastern component) is $P_{1.4\,\rm GHz} = 2.4 \pm 0.2 \times 10^{23}$ W Hz^{-1} and for the relic (north-western component) its $P_{1.4\,\rm GHz} = 2.2 \pm 0.2 \times 10^{23}$ W Hz^{-1}.

A precise calculation of the spectral indexes can be determined when radio structures have been detected at multiple frequencies (see Thierbach et al. 2003 for the Coma cluster, Komissarov & Gubanov 1994 for A1914, Bacchi et al. 2003 for A754, and Feretti et al. 2012 for A2319). In the case of A2146, we have only detected the extended radio emission at 1–2 GHz and can therefore only obtain a rough estimate of the spectral indexes based on this image. In this case, we use the point source subtracted image of Fig. 5 and we only consider data points detected above $3\sigma_{\rm rms}$, where $\sigma_{\rm rms}$ is the local noise level. We estimate α by dividing the total integrated flux of the second Taylor term image (.tt1 image produced with the CLEAN task) with the total integrated flux of the total-intensity image (.tt0 image). This allows us to obtain an estimate of the average spectral index integrated over the entire radio structure. We find a value of $\alpha = 1.2 \pm 0.1$ for the halo (south-east component) and $\alpha = 2.3 \pm 0.3$ for the relic (north-west component), as well as an average value of $\alpha = 1.7 \pm 0.1$ when considering both components. We note that the uncertainty quoted on these values reflects only the uncertainty of the fluxes measured via the.tt1 and.tt0 images. Considering that we are estimating the spectral index based only on the detection of the halo in a very narrow frequency range of 1–2 GHz, the true uncertainty is likely significantly higher. We therefore stress that these are only rough estimates and that a detection at other frequencies is needed to further constrain the spectral index measurements of the radio emission in A2146.

Nonetheless, the derived spectral index of the relic from the VLA 1–2 GHz image ($\alpha \approx 2.3$) is roughly consistent with the expected injection spectral index ($\alpha_{\rm inj}$) predicted by DSA, where

$$\alpha_{\rm inj} = \frac{\mathcal{M}^2 + 1}{\mathcal{M}^2 - 1} - \frac{1}{2}. \quad (2)$$

Indeed, based on deep *Chandra* observations, Russell et al. (2012b) estimate that the Mach number for the upstream shock is $\mathcal{M} = 1.6 \pm 0.1$, which would imply that $\alpha_{\rm inj} \approx 1.8$. However, we stress once more that a better constraint on the spectral index by detecting the relic at other frequencies beyond 1–2 GHz is needed to test this further.

4.3 Properties of the radio halo

In Fig. 7, we show a compilation of radio halo spectral index measurements from the literature (Feretti et al. 2012; Venturi et al. 2013; Bonafede et al. 2014a,b; Knowles et al. 2016). The values are total spectral index values for straight spectra, or low-frequency spectral index values for curved spectra. As shown, most haloes have spectral index measurements of $\alpha \approx$ 1–1.5, but some, known as ultrasteep spectrum radio haloes (USSRHs) and shown in dark grey in Fig. 7, have $\alpha \approx$ 1.6–1.9. These are thought to be the older counterparts of haloes, in which the population of electrons has aged, causing the spectra to steepen even further (e.g. Venturi et al. 2013). The value derived for the spectral index of the halo (south-eastern component) in A2146 (roughly $\alpha_{1-2\,\rm GHz} \approx 1.2$; shown in red in Fig. 7) does not appear to be consistent with the aged population of haloes. We also note that the non-detection of the halo at 325 MHz with the GMRT also implies that the halo must have a low value of the spectral index, roughly $\alpha \approx 1.0$.

Donnert et al. (2013) argue that the properties of haloes in clusters of galaxies vary depending on the stage of the merger. Based on high-resolution magnetohydrodynamic simulations of a 1.5×10^{15} M$_\odot$ cluster with a mass ratio of 1: 8, the authors found that both X-ray and radio luminosities increase during the infall phase (<0.1 Gyr after core passage) and that radio emission is

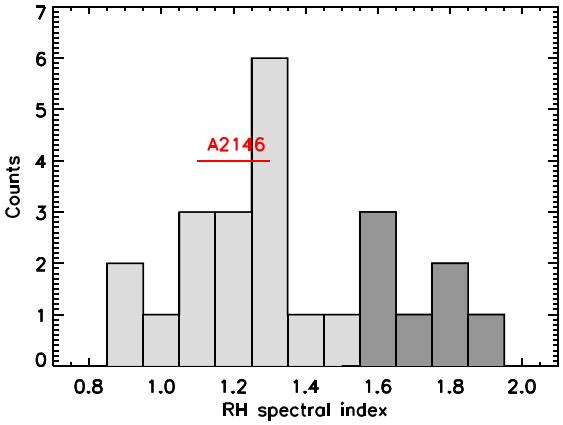

Figure 7. Spectral index measurements (α) of radio haloes, taken from Feretti et al. (2012), Venturi et al. (2013), Bonafede et al. (2014a,b), and Knowles et al. (2016). The dark grey area shows the USSRH sources with $\alpha > 1.6$. Also highlighted is the value of α in A2146, estimated to be roughly 1.2 ± 0.1 based on the VLA 1–2 GHz image.

localized within the shock fronts. Roughly ≈0.1–0.5 Gyr after core passage, the X-ray emission declines due to the decrease in density, while the radio emission continues to increase as turbulence drives the re-acceleration of particles throughout the cluster volume. Finally, >0.5 Gyr after core passage, the radio emission fades significantly and becomes offset from the primary core of the merger, essentially entering a *radio-off* state. In addition to variations of the radio intensity, Donnert et al. (2013) predict that the spectral index of the halo will vary with time, from flat spectra early on ($\alpha \approx 1.0$), down to very steep spectra at late times ($\alpha > 1.5$).

In the case of A2146, Fig. 5 shows that the halo is strongly confined within the bow shock front such that the merger-induced turbulence has not yet reached the entire cluster. We note in particular that the halo appears to be more extended along the eastern direction, even though the bow shock extends to the west (see Fig. 5). This is intriguing given that the temperature map in Fig. 4 shows that there is more mixing (i.e. turbulence) on the eastern side of the bow shock, as opposed to the western side. The halo may also extend to the southern X-ray plume.

In addition, the radio power of the halo is amongst the lowest detected thus far ($P_{1.4\,\mathrm{GHz}} = 2.4 \pm 0.2 \times 10^{23}$ W Hz^{-1}; e.g. Knowles et al. 2016), and our rough estimate of the spectral index based on the VLA image is consistent with the younger population of haloes ($\alpha < 1.5$). All of these observations are consistent with the halo being in a very early stage of formation, roughly ≈0.3 Gyr after core passage according to the simulations of Donnert et al. (2013), although A2146 is thought to be a merger with a much smaller mass ratio of 4–3: 1 (Russell et al. 2010; White et al. 2015) compared to the cluster in the simulations. Interestingly, this falls within the age estimate obtained by White et al. (2015), who used spectroscopic measurements of cluster members to establish the dynamical state of A2146. Based on a two-body dynamical model, the authors estimated that the time-scale after first core passage must be on the order of ≈0.24–0.28 Gyr. We therefore conclude that the radio halo in A2146 is not only amongst the faintest ever detected, but that its properties are also consistent with the halo being in its early stages of formation. This makes the halo in A2146 extremely interesting to study, since it allows us to probe the complete evolutionary stages of haloes.

4.4 Implications for radio haloes

Radio haloes are not ubiquitous in galaxy clusters. Currently, the literature reports the existence of ≈40 haloes (Giacintucci et al. 2017), all of which are identified in massive clusters ($M > >10^{14}$ M$_\odot$). Haloes are thought to originate from the re-acceleration of in situ relativistic particles by turbulence generated from the cluster merger (e.g. Liang et al. 2000; Cassano et al. 2006). Radio haloes may also be produced by inelastic hadronic collisions between cosmic ray protons and thermal protons (see e.g. Dennison 1980), but this scenario is less favoured because of the lack of predicted gamma-ray emission and the existence of USSRHs. For the latter, the hadronic models predict that the relativistic energy would exceed the thermal energy, which is implausible.

Radio haloes are known to exhibit empirical correlations between radio halo power and various thermal cluster properties, including X-ray luminosity, gas temperature, cluster mass, and the cluster integrated Sunyaev–Zel'dovich (SZ) signal (see Cassano et al. 2013, for a recent re-visitation of the relations). Several studies confirm that the correlations exhibit a bimodal distribution, with the X-ray luminous or massive clusters either falling on the correlation or a factor of 2–3 below, known as the *radio-off* state (Venturi et al. 2007, 2008). In the case of A2146, because of the non-detection of the halo in A2146 with the GMRT, Russell et al. (2011) argued that A2146 may not be massive enough to generate a luminous halo, explaining why the cluster falls well below the correlation even if strongly merging. Low-mass systems are expected to generate less turbulence, producing less luminous haloes. If this is the case, radio haloes might therefore be significantly more numerous than thought, but our current view is limited by the sensitivity of radio telescopes (e.g. GMRT and VLA).

In the left-hand panel of Fig. 8, we illustrate the location of the halo in A2146 compared to other clusters for the 1.4 GHz radio halo power versus integrated SZ signal (Y_{500}) within a radius at which the average density is 500 times the critical density at the cluster redshift (R_{500}) from Cassano et al. (2013). Although the X-ray luminosity of the cluster might be boosted during the merger phase, we also show in Fig. 8 (middle panel) the $P_{1.4\,\mathrm{GHz}}$–L_{500} diagram. Here, we use the X-ray luminosity within R_{500} derived by Cassano et al. (2013). We do not show the $P_{1.4\,\mathrm{GHz}}$–M_{500} correlation, since the mass estimate for A2146, given its complex dynamical state, varies significantly from one study to the next: from $M_{500} \approx 3.8 \times 10^{14}$ M$_\odot$ for an SZ estimate with the *Planck* satellite (Planck Collaboration et al. 2014), to $M_{200} = 8.5^{+4.3}_{-4.7} \times 10^{14}M_\odot$ based on a dynamical analysis of the cluster members (White et al. 2015), to $M_{200} = 1.4^{+0.3}_{-0.4} \times 10^{15}M_\odot$ for a *Hubble Space Telescope* weak lensing analysis (King et al. 2016). Instead, we focus on the X-ray luminosity and integrated SZ measurement obtained with the *Planck* satellite ($Y_{500} = 0.000032 \pm 0.000006$ Mpc^2), which is consistent with the value obtained with the Arcminute Microkelvin Imager ($Y_{500} = 0.000029 \pm 0.000014$ Mpc^2, private communication; see also Zwart et al. 2008 and Rodriguez-Gonzalvez et al. 2011). The left-hand panel of Fig. 8 essentially shows that the halo of A2146 is indeed one of the faintest detected thus far. It also appears to be consistent with the $P_{1.4\,\mathrm{GHz}}$–Y_{500} correlation, although offset from the $P_{1.4\,\mathrm{GHz}}$–L_{500} correlation (however, we note that the X-ray luminosity of the cluster might be boosted during the merger phase). We also note that, as argued in Section 4.2, if the halo (south-east component seen in Fig. 5) were actually composed of a halo and a relic, the derived radio power of the halo would be even smaller and A2146 would sit even further below the correlations, still making it one of the faintest ever detected.

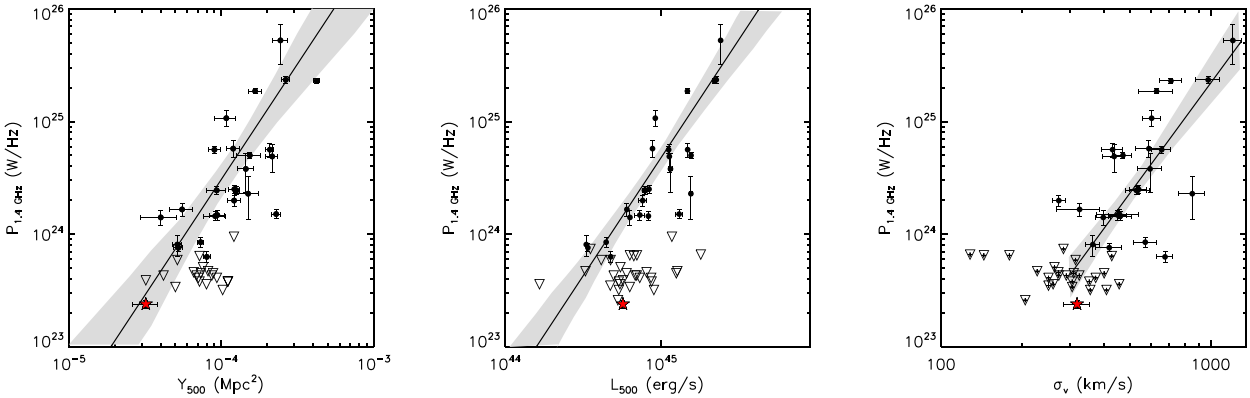

Figure 8. Left:Correlation of the radio halo power at 1.4 GHz ($P_{1.4\,GHz}$) as a function of the integrated SZ signal (Y_{500}) of the cluster within R_{500} (Cassano et al. 2013). USSRHs lie to the right of the correlation. The shaded region shows the 95 per cent confidence level. Middle: Correlation of the radio halo power at 1.4 GHz ($P_{1.4\,GHz}$) as a function of the X-ray luminosity (L_{500}) of the cluster within R_{500}, also from (Cassano et al. 2013). The shaded region also shows the 95 per cent confidence level. Right: Correlation of the radio halo power at 1.4 GHz ($P_{1.4\,GHz}$) as a function of the turbulent velocity measured from the amplitude of density fluctuations (σ_v) for 51 clusters (Eckert et al. 2017). The shaded region shows the 68 per cent confidence region. The halo in A2146 is highlighted with the red star in all three panels.

More recently, Eckert et al. (2017) derived the velocity dispersion of 51 clusters based on the amplitude of density fluctuations and found that the turbulent velocity of the cluster with radio haloes was on average a factor of 2 higher than those without haloes. This result supports the scenario in which haloes are driven by turbulent motions. They also find a strong correlation between radio halo power at 1.4 GHz ($P_{1.4\,GHz}$) and the turbulent velocity (σ_v). These authors include A2146 in their study, for which they find that $\sigma_v = 319 \pm 5\,km\,s^{-1}$. The detection of the candidate halo in A2146 with $P_{1.4\,GHz} = 2.4 \pm 0.2 \times 10^{23}$ W Hz^{-1} places A2146 within the scatter of the correlation observed by Eckert et al. (2017) (see the right-hand panel of Fig. 8).

5 CONCLUDING REMARKS

We have detected a diffuse, radio structure associated with the merging cluster A2146 using deep, multiconfiguration VLA observations at 1–2 GHz (16 h). The radio structure is faint ($P_{1.4\,GHz,\,total} = 4.6 \pm 0.3 \times 10^{23}$ W Hz^{-1}), elongated along the merger axis and strongly confined between both the bow and upstream X-ray shock fronts. This structure extends over 850 kpc in length and appears to harbour multiple components, one associated with the upstream shock that we classify as a radio relic, and another associated with the subcluster core that is consistent as being a radio halo bounded by the bow shock. The latter is amongst the faintest radio haloes detected thus far in the bimodal distributions of radio halo power ($P_{1.4\,GHz}$) versus thermal cluster properties (Y_{500}, L_{500}, M_{500}). We note that the halo could actually be composed of a halo and a second relic that coincides with the bow shock, but the current observations do not allow us to distinguish between possibilities. Future observations, in particular via polarization, could provide a definitive answer. However, if this were the case, then the radio halo would be even fainter.

The spectral index of the halo, derived from the 1–2 GHz VLA image, as well as its non-detection at 325 MHz with the GMRT imply that the structure must have a low value of the spectral index, with $\alpha \approx 1$. The confinement of the halo within the X-ray shock fronts indicates that the merger-induced turbulence has not yet reached the cluster scale and that the halo is most likely in its early stages of formation. The low spectral index and the location of A2146 in the Y_{500}–$P_{1.4\,GHz}$ correlation also suggest that this halo is in its early stages of formation, roughly ≈0.3 Gyr after first core passage, consistent with the dynamical analysis of the cluster members. Such low radio power haloes provide a unique opportunity to study the physical processes that govern the initial stages of halo formation, making the study of faint radio haloes just as important as the study of the luminous radio haloes.

Given that the detection of the extended radio emission in A2146 was only possible through deep VLA observations reaching a noise level of 10 μJy beam^{-1}, i.e. more than an order of magnitude deeper than previous observations, several other radio haloes are bound to be discovered with the next generation of radio telescopes such as the Long Wavelength Array (LWA; Taylor et al. 2012), the Murchison Widefield Array (Lonsdale et al. 2009; Bowman et al. 2013; Tingay et al. 2013), LOFAR (LOw Frequency ARray; van Haarlem et al. 2013), and the upcoming SKA (Square Kilometre Array; Dewdney et al. 2009). Indeed, these telescopes will not only reach even lower noise levels (e.g. SKA is predicted to reach flux densities as least 10 times fainter), but they will also provide the good uv-coverage at short baselines needed to detect extended diffuse emission in clusters. This will be extremely important in light of the faint halo and relic discovered in A2146, and for any similar structures caught in their early stages of formation.

In summary, our results highlight the need for additional deep observations of clusters to better understand the faint end of the bimodal $P_{1.4\,GHz}$ versus thermal property correlations and that many of the clusters in the upper limit region may indeed host faint radio haloes.

ACKNOWLEDGEMENTS

JHL is supported by NSERC through the discovery grant and Canada Research Chair programmes, as well as FRQNT through the new university researchers start up programme. MLGM is supported by NSERC through the NSERC Post-graduate Scholarship Doctoral programme (PGSD). DFB is supported by NSERC, through the summer internship programme. We thank Becky Canning for

helpful discussions about the point sources in the cluster, as well as the cluster members.

REFERENCES

Ackermann M. et al., 2014, ApJ, 787, 18
Bacchi M., Feretti L., Giovannini G., Govoni F., 2003, A&A, 400, 465
Bonafede A., Govoni F., Feretti L., Murgia M., Giovannini G., Brüggen M., 2011, A&A, 530, A24
Bonafede A. et al., 2014a, MNRAS, 444, L44
Bonafede A., Intema H. T., Brüggen M., Girardi M., Nonino M., Kantharia N., van Weeren R. J., Röttgering H. J. A., 2014b, ApJ, 785, 1
Bowman J. D. et al., 2013, PASA, 30, 31
Bradač M. et al., 2006, ApJ, 652, 937
Briggs H., Voges W., Bohringer H., Edge A. C., Huchra J. P., Briel U. G., 1996, MNRAS, 281, 799
Brown S., Emerick A., Rudnick L., Brunetti G., 2011, ApJ, 740, L28
Brunetti G., Jones T. W., 2014, Int. J. Mod. Phys. D, 23, 1430007
Brunetti G., Setti G., Feretti L., Giovannini G., 2001, MNRAS, 320, 365
Canning R. E. A. et al., 2012, MNRAS, 420, 2956
Cassano R., Brunetti G., Setti G., 2006, MNRAS, 369, 1577
Cassano R. et al., 2013, ApJ, 777, 141
Clowe D., Gonzalez A., Markevitch M., 2004, ApJ, 604, 596
Clowe D., Bradač M., Gonzalez A. H., Markevitch M., Randall S. W., Jones C., Zaritsky D., 2006, ApJ, 648, L109
Cohen A. S., Lane W. M., Cotton W. D., Kassim N. E., Lazio T. J. W., Perley R. A., Condon J. J., Erickson W. C., 2007, AJ, 134, 1245
Coleman J. E. et al., 2017, MNRAS, 464, 2469
Condon J. J., Cotton W. D., Greisen E. W., Yin Q. F., Perley R. A., Taylor G. B., Broderick J. J., 1998, AJ, 115, 1693
Cornwell T. J., Golap K., Bhatnagar S., 2005, in Shopbell P., Britton M., Ebert R., eds, ASP Conf. Ser. Vol. 347, Astronomical Data Analysis Software and Systems XIV. Astron. Soc. Pac., San Francisco, p. 86
Dennison B., 1980, ApJ, 239, L93
Dewdney P. E., Hall P. J., Schilizzi R. T., Lazio T. J. L. W., 2009, IEEE, 97, 1482
Donnert J., Dolag K., Brunetti G., Cassano R., 2013, MNRAS, 429, 3564
Drury L. O., 1983, Rep. Prog. Phys., 46, 973
Eckert D., Gaspari M., Vazza F., Gastaldello F., Tramacere A., Zimmer S., Ettori S., Paltani S., 2017, ApJ, 843, L29
Ensslin T. A., Biermann P. L., Klein U., Kohle S., 1998, A&A, 332, 395
Feretti L., Giovannini G., Govoni F., Murgia M., 2012, A&AR, 20, 54
Giacintucci S., Markevitch M., Cassano R., Venturi T., Clarke T. E., Brunetti G., 2017, ApJ, 841, 71
Haslam C. G. T., Salter C. J., Stoffel H., Wilson W. E., 1982, A&AS, 47, 1
Hogan M. T. et al., 2015, MNRAS, 453, 1201
Intema H. T., Jagannathan P., Mooley K. P., Frail D. A., 2017, A&A, 598, A78
Jeltema T. E., Profumo S., 2011, ApJ, 728, 53
King L. J. et al., 2016, MNRAS, 459, 517
Knowles K. et al., 2016, MNRAS, 459, 4240
Komissarov S. S., Gubanov A. G., 1994, A&A, 285, 27
Liang H., Hunstead R. W., Birkinshaw M., Andreani P., 2000, ApJ, 544, 686
Lonsdale C. J. et al., 2009, IEEE, 97, 1497
Macario G., Markevitch M., Giacintucci S., Brunetti G., Venturi T., Murray S. S., 2011, ApJ, 728, 82
Markevitch M., 2010, preprint (arXiv:1010.3660)
Markevitch M., Vikhlinin A., 2001, ApJ, 563, 95
Markevitch M., Gonzalez A. H., David L., Vikhlinin A., Murray S., Forman W., Jones C., Tucker W., 2002, ApJ, 567, L27
Markevitch M., Gonzalez A. H., Clowe D., Vikhlinin A., Forman W., Jones C., Murray S., Tucker W., 2004, ApJ, 606, 819
Markevitch M., Govoni F., Brunetti G., Jerius D., 2005, ApJ, 627, 733
Miller N. A., Owen F. N., 2003, AJ, 125, 2427
Mohan N., Rafferty D., 2015, Astrophysics Source Code Library, record ascl:1502.007
O'Dea C. P., 1998, PASP, 110, 493
Ogrean G. A., Brüggen M., 2013, MNRAS, 433, 1701
Owen F. N., Rudnick L., Eilek J., Rau U., Bhatnagar S., Kogan L., 2014, ApJ, 794, 24
Owers M. S., Randall S. W., Nulsen P. E. J., Couch W. J., David L. P., Kempner J. C., 2011, ApJ, 728, 27
Petrosian V., 2001, ApJ, 557, 560
Planck Collaboration XXIX, 2014, A&A, 571, A29
Poggianti B. M., Bridges T. J., Komiyama Y., Yagi M., Carter D., Mobasher B., Okamura S., Kashikawa N., 2004, ApJ, 601, 197
Rau U., Cornwell T. J., 2011, A&A, 532, A71
Rodriguez-Gonzalvez C. et al., 2011, MNRAS, 414, 3751
Russell H. R., Sanders J. S., Fabian A. C., Baum S. A., Donahue M., Edge A. C., McNamara B. R., O'Dea C. P., 2010, MNRAS, 406, 1721
Russell H. R. et al., 2011, MNRAS, 417, L1
Russell H. R., Fabian A. C., Taylor G. B., Sanders J. S., Blundell K. M., Crawford C. S., Johnstone R. M., Belsole E., 2012a, MNRAS, 422, 590
Russell H. R. et al., 2012b, MNRAS, 423, 236
Shimwell T. W., Brown S., Feain I. J., Feretti L., Gaensler B. M., Lage C., 2014, MNRAS, 440, 2901
Taylor G. B. et al., 2012, J Astron. Instrum., 1, 1250004
Thierbach M., Klein U., Wielebinski R., 2003, A&A, 397, 53
Tingay S. J. et al., 2013, PASA, 30, 7
van Haarlem M. P. et al., 2013, A&A, 556, 2
van Weeren R. J., Röttgering H. J. A., Brüggen M., Hoeft M., 2010, Science, 330, 347
van Weeren R. J., Brüggen M., Röttgering H. J. A., Hoeft M., 2011, MNRAS, 418, 230
van Weeren R. J. et al., 2014, ApJ, 786, L17
van Weeren R. J. et al., 2016, ApJ, 818, 204
van Weeren R. J. et al., 2017, Nature Astron., 1, 0005
Venturi T., Giacintucci S., Brunetti G., Cassano R., Bardelli S., Dallacasa D., Setti G., 2007, A&A, 463, 937
Venturi T., Giacintucci S., Dallacasa D., Cassano R., Brunetti G., Bardelli S., Setti G., 2008, A&A, 484, 327
Venturi T., Giacintucci S., Dallacasa D., Cassano R., Brunetti G., Macario G., Athreya R., 2013, A&A, 551, A24
White J. A. et al., 2015, MNRAS, 453, 2718
Zwart J. T. L. et al., 2008, MNRAS, 391, 1545

This paper has been typeset from a TEX/LATEX file prepared by the author.